Projectile Ascent Trajectory Using Moving Mass Control

by
Berit Syltebo

A thesis submitted in partial fulfillment
of the requirements for the degree of

Master of Science
in Aeronautics & Astronautics

UNIVERSITY OF WASHINGTON
2024

Committee:
Mehran Mesbahi
Dana Dabiri

Program authorized to offer degree:
Aeronautics & Astronautics

University of Washington

Abstract

Projectile Ascent Trajectory Using
Moving Mass Control

Berit Syltebo

Chair of the supervisory committee:
Mehran Mesbahi
Aeronautics & Astronautics

The current best technology to reach orbit is rocketry - but there may be under-explored solutions that provide cheaper, less complex, and more environmentally-friendly access to space. Impulse launchers have the potential to achieve these three criteria. This study seeks to control such an ascent vehicle - originating from a linear impulse launcher - using a moving mass as the sole source of actuation. The system non-linearities necessitate the use of gain scheduling to account for the vast changes in Mach number and altitude. A gain-scheduled PID control look-up table is constructed under a list of time and frequency domain stability criteria. Two potential ascent trajectories are explored: an aggressive approach which minimizes vehicle mass and ascent time, and an orbit-conscious approach which minimizes the velocity correction requirement to enter orbit. Simulations provide a proof of concept for vehicles achieving orbital velocities at the Karman Line when launched at Mach 30. However, limitations in effectiveness at high altitudes prevent the vehicle from entering orbit with a moving mass alone.

Acknowledgments

I would like to express my deepest gratitude to all those who have contributed to the completion of this thesis.

First, I am extremely grateful to Longshot Space Technologies Corporation for their generous funding and support of my research. This work would not have been possible without their financial assistance and resources.

I would also like to thank my thesis advisor, Professor Mehran Mesbahi, for his invaluable guidance, insightful advice, and constant encouragement throughout the duration of my research. His expertise and dedication have been instrumental in shaping this project and my growth as a researcher.

Additionally, I wish to extend my sincere thanks to all members of UW RAIN Lab. Your camaraderie, collaborative spirit, and unwavering support have made this journey both productive and enjoyable. The many discussions, brainstorming sessions, and shared challenges have significantly enriched my research experience.

Finally, I am grateful to my family and friends for their endless support and patience. Your belief in me has been a source of strength throughout this endeavor.

Thank you all for your contributions and support.

Contents

List of Figures

List of Tables

Chapter 1

Introduction

It is no secret that rocketry is the dominating technology used for space access. The spectacle has captured the imaginations of current and future engineers and researchers since the extensive worldwide government efforts dating back to the 1950's. Its' sci-fi level complexity coined the phrase "it's not rocket science", sparking inspiration across generations. Presently, space access technology development has spread to private corporations like SpaceX and Blue Origin, honing and perfecting all that is known about ascent vehicles to broaden the possibilities of space missions.

This sparks an important question: with all eyes on rockets, is it possible that other solutions to space access - possibly superior in influential performance metrics - have been set aside and neglected for the sake of rocket development? One such solution may be direct space launch. Instead of relying on transporting fuel during ascent, the idea behind this emerging technology is to give a projectile or ascent vehicle all the momentum is needs on the ground to reach space. By mass, only 9% of the Saturn V rocket was capable of achieving Low Earth Orbit because the other 91% was stored potential energy at liftoff and depleted during ascent. In contrast, an ascent vehicle originating from direct launch will carry almost its entire mass to space with the exception of heat shield ablation effects; percentages will depend on surface area, volume, mass, and trajectory.

In the past decade, a number of private and public institutions have begun to tackle this problem. This includes private start-ups like SpinLaunch, Wave Motion, and Longshot Space Technologies Corporation, as well as public research facilities like University of Washington's Ram Accelerator [12]. All of which occupy a different method of impulse launching. Some claim that successful development and implementation will provide space access services that are cheaper, more environmental friendly, and less complex than tried-and-true rocketry.

1.1 Impulse Launching - Longshot Space

One such company is Longshot Space Technologies Corporation based in Oakland, California. Longshot boasts an impressive speed record of Mach 4.3 from their 80-

foot-long linear impulse launcher, developed from government and private investor funding, and believe that hypersonic (Mach 5) is within reach.

While this form of technology is new to the space industry, it has been applied in the defense industry dating back to the 1800s. The V-3 (Vengeance Weapon 3) canon was developed for the German offensive during World War II, permanently aiming at London, England [5]. Having a fixed heading, the V-3 was deemed rather ineffective in comparison to its V-1 and V-2 counterparts whose guiding technologies proved far superior. Multi-stage projectile-accelerating technologies never became a prominent military tool.

It is possible, however, that there is potential for inexpensive and repetitive space launch - this is Longshot's mission. The ultimate goal is to develop a 6-mile-long canon capable of accelerating a projectile from 0 to Mach 30 using only compressed air and running on solar energy. Pressure gradients are responsible for the impressive acceleration, completely eliminating the need for combustion. Due to the large gravitational loads the projectile will experience, the concept is aimed toward durable payloads such as satellites and is far from suitable for human space flight.

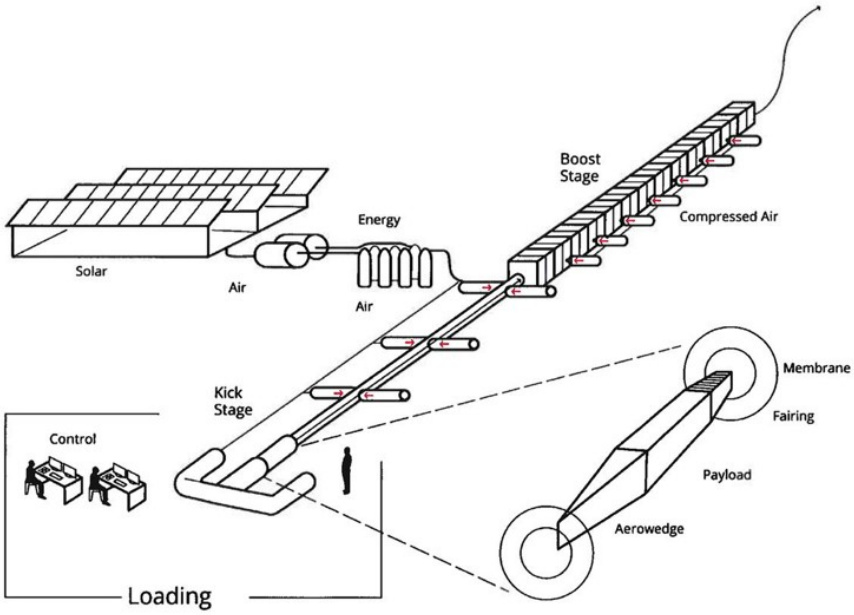

Figure 1.1: Diagram of Longshot Space Technology's concept impulse launcher [4]

Figure 1.1 shows a concept drawing of the future space launch system Longshot is hoping to achieve. The projectile will house the payload and is responsible for transportation to space while sustaining the extreme conditions Earth atmosphere will inevitably present.

The kick stage will provide the initial boost, accelerating the projectile from 0. The 6-mile barrel itself will be pulled vacuum while the kick stage will house highly pressurized air; the two regions will be separated by a burst disk rated to some desired failure. Upon failure, the pressurized air will quickly accelerate into the low-pressure

region providing a strong force on the projectile down the barrel as a result of the pressure gradient. This initiates launch.

As the projectile travels down the barrel, it will pass a series of boosters responsible for continuing the acceleration process - this is multi-stage projectile acceleration. At a certain point, the effects of pressure gradients and gas expansion become inadequate in the journey to Mach 30. In this clever design, boosters are injected normally to the barrel on either side such as to 'squeeze' the aerowedge serving as the tail on the projectile. Depending on the angle of this wedge, for every unit length the booster air travels, the projectile must move forward by a larger amount. This technology will be designed to achieve Mach 30.

1.2 Moving Mass Control

Moving mass control (MMC) is an emerging control method in aerospace, primarily with the application of controlling pitch and attitude of unmanned aerial vehicles [14]. In astronautical systems, such as satellites, MMC is effective in achieving desired attitudes while protecting instrumentation within the vessel. In one such study [10], the use of three moving masses within a satellite were used to achieve precision pointing such that the angular momentum of the entire system is zero. In aeronautics, MMC can be used for either attitude or pitch control due to the presence of atmosphere. Such applications include the pitch and yaw control of quadrotors [9] where torques are produced through the change in center of gravity rather than propulsive control, and longitudinal mass displacement along long endurance aircraft [8].

The motivation behind MMC in this study is the elimination of external control surfaces. This, in turn, eliminates a major engineering design challenge because all control hardware is housed in the chassis of the projectile. The extreme environment the projectile will be subjected to poses a large enough challenge in heat shield design, let alone external control surface.

The ascent vehicle described in this paper will solely use MMC for pitch control, similar to MMC research on fixed-wing aircraft [11]. The aerodynamic forces on a body act through the center of pressure while all moments act around the center of gravity. When these two key locations don't line up with the incoming flow, the aerodynamic forces apply a torque about the body as a function of the distance between the aforementioned points. The application of MMC in this study is to change the center of gravity such that the necessary torques are applied to achieve the desired angle of attack at any given time. This allows the projectile to track a trajectory.

1.3 Research Goals & Previous Work

At the time of publication of this thesis, there has been a lot of work developing accelerators for direct space launch but there has been very little on the projectile

and what happens to it after ejection. Reaching space is still a very big question and will present several engineering challenges that have yet to be solved. Most notably, the fastest man-made aircraft was NASA's X-43 clocked at Mach 9.6. This number is much smaller than the intended Mach 30. Current structural and heat shield ablation technology is far from sufficient to withstand the temperature and pressures intended for a direct launch ascent vehicle of this nature.

Despite the long list of challenges, if this is ever to become a reality, someone needs to start working on answers. This thesis strives to provide a baseline for controls solutions and a proof of concept for moving mass control. The exploratory nature leaves many open-ended questions to a very complex and multi-dimensional problem, but the work presented in this paper seeks to motivate a general road map for future work.

Under many assumptions and simplifications, a simulation is constructed to simulate and compare possible trajectories using moving mass as the sole form of actuation. This actuation type has been explored in various aerial applications in other research projects which provides a starting point for much of this work. In 2023, researchers out of China [8] developed a moving mass control scheme for a high-altitude long-endurance (HALE) unmanned aerial vehicle (UAV) which primarily investigates longitudinal dynamics. The study showed a dramatic increase in control efficiency compared to the leading actuation type, elevator deflection, in simulation. In 2004, researchers out of California and Virginia [16] developed a 9 degree of freedom (9DOF) kinetic warhead model utilizing moving mass control along all three axes. The interception of a variety of targets are explored including those which are capable of unknown maneuvers.

The simulation proposed in this thesis provides an extension of the above work to direct space launch. Only longitudinal dynamics are captured. The limitations of moving mass as the sole actuation is explored with the absence of propulsive forces.

1.4 Thesis Overview

The outline of the thesis is as follows: Chapter 2 introduces and derives the dynamics of the projectile. The nonlinear dynamics are first presented in the flat Earth frame before a quick transformation to the Earth-centered inertial (ECI) frame such that the curvature of the Earth is captured. Interactions with the atmosphere are explored such that an aerodynamic model is developed using oblique shock wave theory. Atmospheric data is drawn directly from the International Standard Atmosphere (ISA) model. Chapter 3 covers the development of the gain-scheduled PID controller used in simulation to track reference trajectories. The linearized dynamics motivate the otherwise empirical tune of each gain set. Performance of the controller is tested against the specified stability criteria. Chapter 4 discusses how the studies in previous sections come together to form one MATLAB Simulink simulation tool. Chapter 5 presents the results of this thesis; specifically, sample trajectories to space and an investigation of optimization variables. The sample trajectories include an aggressive

approach and orbit-conscious approach. Finally, next steps are discussed in Chapter 6. Short- and long-term tasks are recognized as well as suggestions for priority projects.

Chapter 2

Dynamical Model

This chapter explores the derivation of the dynamical model and the scientific data required to approximate reality. The nonlinear, two-dimensional dynamics are derived to define the longitudinal motion of the projectile. This is first presented in the flat Earth frame for simplicity, and then modified to account for the curvature of the Earth using orbital mechanics.

The resulting equations of motion necessitate a deeper understanding of atmospheric effects. First, by approximating the geometry of the projectile as a wedge, an aerodynamic model is constructed using oblique shock wave theory. The non-dimensional axial and normal force coefficients allow for the computation of body forces given wedge dimensions and properties of the immediate atmosphere. Thus, a comprehensive atmospheric model is constructed to capture important characteristics up to the Karman line. The presented data is drawn from the official International Standard Atmosphere (ISA) model.

2.1 Derivation of Equations of Motion

2.1.1 Flat Earth Frame

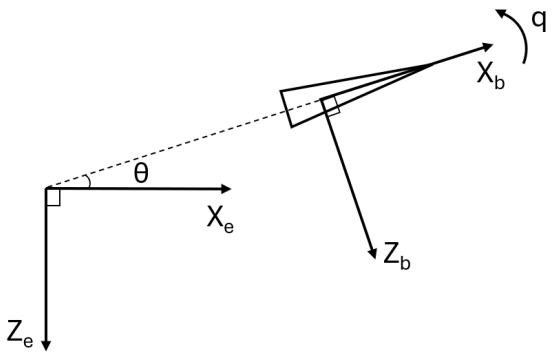

Figure 2.1: Flat Earth and body frames with respect to airborn projectile

The two-dimensional, three-degree-of-freedom (3DOF) equations of motion in the flat Earth frame are represented by the set of Equations 2.1 - 2.8 as defined in [1]. The two frames represented are the flat Earth frame and body frame as shown in Figure 2.1.

$$\dot{X}_e = u\cos\theta + w\sin\theta \tag{2.1}$$
$$\dot{Z}_e = -u\sin\theta + w\cos\theta \tag{2.2}$$
$$A_x^e = \frac{F_x}{m} - g\sin\theta \tag{2.3}$$
$$A_z^e = \frac{F_z}{m} + g\cos\theta \tag{2.4}$$
$$A_x^b = \dot{u} = A_x^e - qw \tag{2.5}$$
$$A_z^b = \dot{w} = A_z^e + qu \tag{2.6}$$
$$\dot{\theta} = q \tag{2.7}$$
$$\dot{q} = \frac{M_y}{I_{yy}} \tag{2.8}$$

The external forces include axial F_x and normal F_z forces with respect to the Earth frame and a moment M_y about the out-of-plane axis. For now, these are purely derived from aerodynamic forces on the body. The moment is obtained by the position of the center of gravity (CG) assuming a fixed center of pressure (CP).

The CP is the point at which aerodynamic forces act through while the body rotates about the CG. Knowing these two locations and the aerodynamic forces, the moment can be obtained per Equation 2.9.

$$M_y = F_z^b(x_{cp} - x_{cg}) + F_x^b z_{cg} \tag{2.9}$$

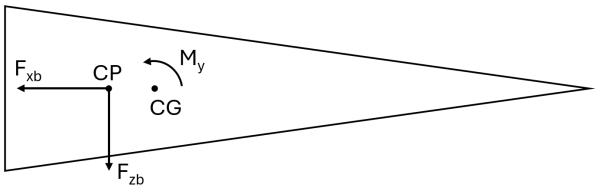

Figure 2.2: External forces with respect to CP and CG

A coordinate transformation is performed to obtain F_x and F_z from the axial and normal forces on the projectile:

$$F_x = F_x^b\cos\theta + F_z^b\sin\theta \tag{2.10}$$
$$F_z = -F_x^b\sin\theta + F_z^b\cos\theta \tag{2.11}$$

2.1.2 Earth Centered Inertial Frame

While the flat Earth frame is generally appropriate for subsonic aircraft, motion is not always fully captured in the hypersonic regime. The curvature of Earth must be considered such that appropriate modifications are made to the equations of motion. Equations 2.3 and 2.4 are rewritten to obtain Equations 2.12 and 2.13 such that the gravitational acceleration is a function of the position of the projectile.

$$A_x^e = \frac{1}{m}\left(F_x + F_{gx}\right) \tag{2.12}$$

$$A_z^e = \frac{1}{m}\left(F_z + F_{gz}\right) \tag{2.13}$$

Orbital Mechanics

The gravitational components are computed using Newton's Law of Gravitation in Equation 2.14 where μ is the gravitational constant of Earth, m is the mass of projectile, and $\vec{r}_e$ is the position vector of the projectile with respect to the Earth center [17]. This is illustrated in Figure 2.3.

$$\begin{bmatrix} F_{gx} \\ F_{gz} \end{bmatrix} = \frac{-\mu m}{|\vec{r}_e|^3} \begin{bmatrix} X_e \\ Z_e \end{bmatrix} \tag{2.14}$$

This modification ensures that the gravitational force vector is always pointed toward the center of the Earth, assuming a perfectly circular body.

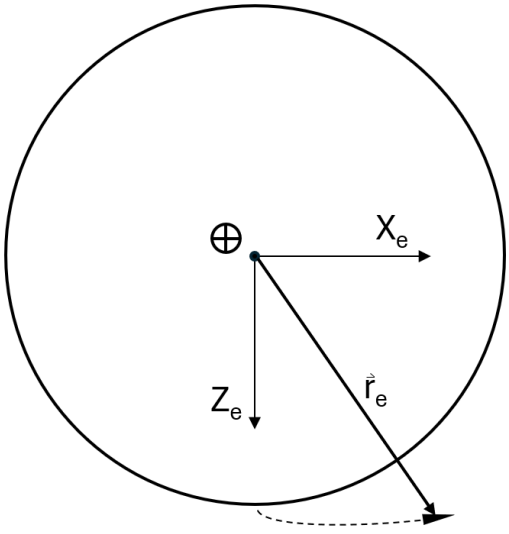

Figure 2.3: Two-dimensional Earth centered inertial Frame with projectile position vector

This gives rise to the importance of understanding the necessary velocity for orbit. The final destination for the projectile is Low Earth Orbit (LEO) which is defined

as an orbit below 2000km altitude; these can be as low as 160km but is typically no lower than 250km in practice. A simple calculation reveals this necessary speed [17]:

$$V^* = \sqrt{\frac{GM}{r}} \tag{2.15}$$

where G is the gravitational constant, M is the mass of the Earth, and r is the orbital radius (radius of Earth plus the orbital altitude). Equation 2.15 assumes a perfectly circular orbit, two-body motion, and is suitable for altitudes with negligible aerodynamics. It yields the following approximation for LEO.

$$V^*_{LEO} \approx 7 \text{ km/s}$$

This will later be used as a design criteria for simulations.

2.2 Projectile Aerodynamic Model

2.2.1 Oblique Shock Wave Theory

In subsonic and hypersonic flows, a shock forms around the projectile. The anatomy of this oblique shock wave is illustrated in Figure 2.4. Upstream of the shock in the free stream, the flow is unperturbed. However, across the shock, the flow experiences a dramatic increase in pressure, density, and temperature, and a decrease in Mach number. Assuming that the shock is attached, the streamlines downstream are parallel to the surface of the wedge such that the deflection angle is equal to the semi-apex of the wedge. Exact theory can be used to determine the 2D wedge aerodynamics.

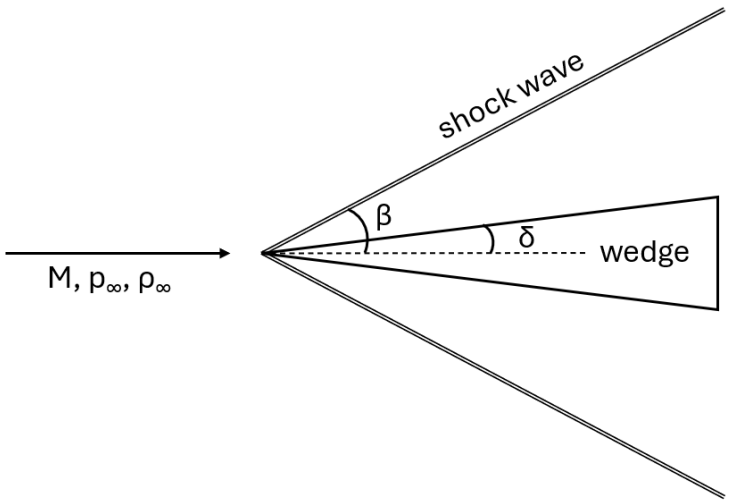

Figure 2.4: Illustration of attached shock wave over a wedge

To compute the coefficient of pressure C_p over a wedge, oblique shock wave theory as described in [18] is used. It is defined [6] as

$$C_p \equiv \frac{p - p_\infty}{q_\infty} = \frac{2}{\gamma M_\infty^2} \cdot \frac{p - p_\infty}{p_\infty} \tag{2.16}$$

where

$$q_\infty = \frac{1}{2}\rho_\infty V_\infty^2 = \frac{\gamma p_\infty}{2} M_\infty^2 \tag{2.17}$$

The oblique sock relation - to account for the projectile geometry - is shown in Equation 2.18, where β is the wave angle and region 1 is upstream of the shock wave.

$$\frac{p_2 - p_1}{p_1} = \frac{\gamma}{\gamma + 1}(M_1^2 \sin^2 \beta - 1) \tag{2.18}$$

Then, the coefficient of pressure can be rewritten as

$$C_p = \frac{2}{\gamma M_\infty^2} \cdot \frac{p - p_\infty}{p_\infty} = \frac{4}{M_\infty^2(\gamma + 1)}(M_\infty^2 \sin^2 \beta - 1) \tag{2.19}$$

where the relation between deflection angle δ, wave angle, and upstream Mach number is given by

$$\tan \delta = 2 \cot \beta \frac{M_\infty^2 \sin^2 \beta - 1}{M_\infty^2(\gamma + \cos 2\beta) + 2} \tag{2.20}$$

An abbreviated tabulation of theoretical aerodynamic data is given in Table 2.1 for various angles of attack, α. Note that at $\alpha = 0°$, the pressure is the same on the upper and lower surfaces of the wedge. However, at nonzero angle of attack, these differ such that C_p is different across these surfaces. As such, they are computed separately with

$$\delta = \delta^\star \pm \alpha \tag{2.21}$$

where $\delta^\star$ is the actual semi-apex angle of the wedge.

In order for this to be useful, the axial and normal force coefficients must be computed. This transformation is simply

$$C_x = \frac{1}{c}\int_0^c \left(C_{p,u}\frac{dy_u}{dx} - C_{p,l}\frac{dy_l}{dx} \right) dx \tag{2.22}$$

$$C_z = \frac{1}{c}\int_0^c (C_{p,l} - C_{p,u}) dx \tag{2.23}$$

Solving the integral for a wedge:

$$C_x = (C_{p,l} + C_{p,u}) \sin \delta^\star \tag{2.24}$$

$$C_z = C_{p,l} - C_{p,u} \tag{2.25}$$

	$\alpha = 0°$	$\alpha = 2°$		$\alpha = 4°$	
Mach	C_p	C_{pl}	C_{pu}	C_{pl}	C_{pu}
2	0.2523	0.3173	0.1928	0.3884	0.1382
6	0.1059	0.1404	0.0761	0.1798	0.05101
10	0.0868	0.1190	0.0598	0.1565	0.0380
14	0.0803	0.1121	0.0540	0.1492	0.0331
18	0.0774	0.1090	0.0513	0.1460	0.0307
22	0.0758	0.1074	0.0498	0.1443	0.0293
26	0.0749	0.1064	0.0489	0.1433	0.0285
30	0.0743	0.1058	0.0483	0.1427	0.0280

Table 2.1: Tabulated theoretical data of the coefficient of pressure over a 20° wedge

Knowing the state of the projectile, the atmospheric forces in the body frame are obtained using Equations 2.26 and 2.27. Here, S is the cross-sectional area of the projectile normal to the free-stream flow.

$$F_x^b = C_x q S \tag{2.26}$$

$$F_z^b = C_z q S \tag{2.27}$$

Running Table 2.1 (with the exception of Mach 2) through the above equations yields the plots in Figure 2.5. The most change with Mach occurs at smaller Mach values but as the projectile becomes more and more hypersonic, C_x and C_z tend to change very little. It is important to note that C_z changes very little with Mach number for the entire horizon considered.

For simulation purposes, the oblique shock wave theory presented above is used as the aerodynamic look-up table that the feedback loop accesses with each pass. There is an obvious limitation that Mach number is not a legitimate quantity in space due to the lack of atmosphere. However, this also means negligible aerodynamic forces for short-term simulation. This problem is considered later in this paper.

2.3 Atmosphere Model

The atmospheric model used in all simulations is taken from the International Standard Atmosphere (ISA) database [2]. Figure 2.6 shows how important atmospheric variables change with altitude, including temperature, speed of sound, pressure, and density. This also highlights the four distinct layers of the atmosphere from sea level to the Karman line (100 km): troposphere, stratosphere, mesosphere, and thermosphere.

The database used is limited to the top of the mesosphere where aerodynamics become negligible for short term missions. This limits the scope of the proceeding designs and necessitates the design condition that the projectile must be able to reach

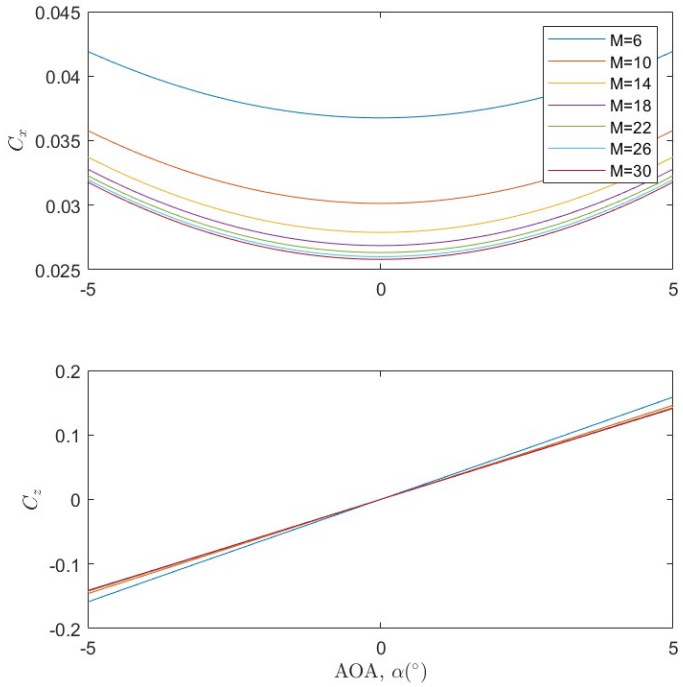

Figure 2.5: Axial (C_x) and normal (C_z) force coefficients on a 20° wedge

an orbit from the top of the mesosphere. Since the aerodynamics are so small, the moving mass system becomes useless except for attitude adjustments. Other systems - outside the scope of this project - are needed to obtain an orbit that does not intersect the Earth's atmosphere on its next pass.

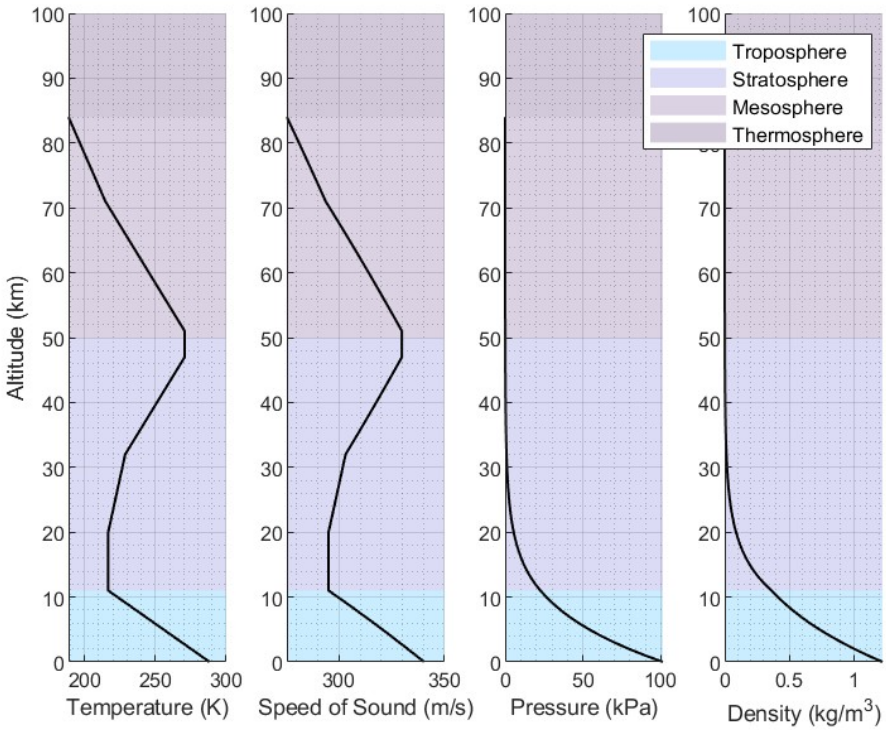

Figure 2.6: Common atmospheric measurements as a function of altitude, according to the ISA

Chapter 3

Control

With the dynamics specified, an appropriate controller is ready for design. This chapter discusses the design process for a gain-scheduled PID controller [13] capable of tracking a planned trajectory from sea level to space.

To aid the initial design and better analyze stability characteristics, a linear model is derived from the nonlinear. This allows for a more comprehensive and accurate understanding of the stability properties and can be useful in obtaining appropriate PID gain values. This leads to a surface level discussion of PID controller mechanics. This feedback control technique is explored through basic block diagram logic flow, followed by a brief discussion of mathematical modelling.

Finally, the benefits of gain-scheduling are discussed alongside real simulations which reveal why this system necessities something more dynamic and adaptable than a standard PID controller. Stability criteria are then established such that a comprehensive gain look-up table is constructed and ready for simulation.

3.1 Derivation of State Space Model

In order for the true nonlinear dynamics to be useful from a controls perspective, they must be linearized. Working in two dimensions, the longitudinal dynamics are adapted per the analysis performed in [7]. [8] presents an adaptation specifically for a moving mass projectile - in their case, a kinetic warhead. These have been further simplified to reflect a projectile with no thrust, where the only source of actuation is the moving mass position.

The state vector becomes

$$X = \begin{bmatrix} u & \alpha & q & \theta \end{bmatrix}$$

with the control vector $U = z_{cg}$. Other state vectors can be chosen depending on the desired controlled variable. In this paper, angle of attack α is the controlled quantity making the proposed vector suitable.

Equation 3.1 is derived by taking the Jacobians of the nonlinear dynamics with respect to the state and control vectors, as described below.

$$A = \frac{\partial f}{\partial X} = \begin{bmatrix} \frac{\partial \dot{u}}{\partial u} & \frac{\partial \dot{u}}{\partial \alpha} & \frac{\partial \dot{u}}{\partial q} & \frac{\partial \dot{u}}{\partial \theta} \\ \frac{\partial \dot{\alpha}}{\partial u} & \frac{\partial \dot{\alpha}}{\partial \alpha} & \frac{\partial \dot{\alpha}}{\partial q} & \frac{\partial \dot{\alpha}}{\partial \theta} \\ \frac{\partial \dot{q}}{\partial u} & \frac{\partial \dot{q}}{\partial \alpha} & \frac{\partial \dot{q}}{\partial q} & \frac{\partial \dot{q}}{\partial \theta} \\ \frac{\partial \dot{\theta}}{\partial u} & \frac{\partial \dot{\theta}}{\partial \alpha} & \frac{\partial \dot{\theta}}{\partial q} & \frac{\partial \dot{\theta}}{\partial \theta} \end{bmatrix}, \qquad B = \frac{\partial f}{\partial U} = \begin{bmatrix} \frac{\partial \dot{u}}{\partial z_{cg}} \\ \frac{\partial \dot{\alpha}}{\partial z_{cg}} \\ \frac{\partial \dot{q}}{\partial z_{cg}} \\ \frac{\partial \dot{\theta}}{\partial z_{cg}} \end{bmatrix}$$

$$A = \begin{bmatrix} X_u & X_w V_a^* \cos\alpha^* & X_q & -g\cos\theta^* \\ \frac{Z_u}{V_a^* \cos\alpha^*} & Z_w & \frac{Z_q}{V_a^* \cos\alpha^*} & \frac{-g\cos\theta^*}{V_a^* \cos\alpha^*} \\ M_u & M_w V_a^* \cos\alpha^* & M_q & 0 \\ 0 & 0 & 1 & 0 \end{bmatrix} \qquad B = \begin{bmatrix} X_{x_1^b} \\ \frac{Z_1^b}{V_a^* \cos\alpha^*} \\ M_{x_1^b} \\ 0 \end{bmatrix} \tag{3.1}$$

The state space in Equation 3.1 appears with a slew of coefficients made up of control and stability derivatives; all of which are defined in Table 3.1. Many of the derivatives can be numerically tabulated from the oblique shock wave aerodynamic coefficient data described in Section 2.2. These include C_{X_0}, C_{X_α}, C_{Z_0}, C_{Z_α}, C_{M_0}, C_{M_α}, and $C_{M_{x_1^b}}$. The rest require approximations.

C_{M_q} can be computed using the pitch damping derivative approximation in Equation 3.2. For the sake of this analysis, C_{X_q} and C_{Z_q} are assumed to be 0. Although this is not a perfect approximation, it is appropriate for some conditions such as subsonic regimes and sleek projectiles. Experimental data is required to better capture these coefficients.

$$C_{M_q} \approx C_{Z_\alpha} \frac{c}{2V_a^*} \tag{3.2}$$

To verify that the nonlinear dynamics are captured, a simulation was conducted to compare the step response behaviors between the linear and nonlinear models (see Figure 3.1). It is clear that there is some deviation between the responses, indicating that the linear model is imperfect. While the settling times are very similar, the nonlinear model appears to have higher damping and a lower natural frequency.

This error can be attributed to a number of factors. The first being the approximations required to compute some of the stability and control derivatives. Without exact experimental data, it must be assumed that there is some non-negligible error capable of affecting the linear model performance. Another potential source of error is tabulation tolerances for the rest of the stability and control derivatives. These are merely estimates based on the C_x and C_z data, and it is assumed that the definition of these computations may have small affects on the linear system. Further, it is possible that the linear model construction neglects important non-linearities and a more thorough understanding of the actual system is required. This discussion assumes that the nonlinear model is correct.

$$X_u = \frac{u^*\rho S}{m}\left[C_{X_0} + C_{X_\alpha}\right] - \frac{\rho S w^* C_{X_\alpha}}{2m}$$

$$X_w = -q^* + \frac{w^*\rho S}{m}\left[C_{X_0} + C_{X_\alpha}\right] + \frac{\rho S u^* C_{X_\alpha}}{2m}$$

$$X_q = -w^* + \frac{\rho V_a^* S c C_{X_q}}{4m}$$

$$Z_u = q^* + \frac{u^*\rho S}{m}\left[C_{Z_0} + C_{Z_\alpha}\right] - \frac{\rho S w^* C_{Z_\alpha}}{2m}$$

$$Z_w = \frac{w^*\rho S}{m}\left[C_{Z_0} + C_{Z_\alpha}\right] + \frac{\rho S u^* C_{z_\alpha}}{2m}$$

$$Z_q = u^* + \frac{\rho V_a^* S c C_{z_q}}{4m}$$

$$M_u = \frac{u^*\rho S c}{I_{yy}}\left[C_{M_0} + C_{M_\alpha}\alpha^* + C_{M_{x_1^b}} x_1^{b*}\right] - \frac{\rho S c w^* C_{M_\alpha}}{2I_{yy}}$$

$$M_w = \frac{w^*\rho S c}{I_{yy}}\left[C_{M_0} + C_{M_\alpha}\alpha^* + C_{M_{x_1^b}} x_1^{b*}\right] - \frac{\rho S c u^* C_{M_\alpha}}{2I_{yy}}$$

$$M_q = \frac{\rho V_a^* S c^2 C_{M_q}}{4I_{yy}}$$

$$M_{x_1^b} = \frac{\rho V_a^{2*} S c C_{M_{x_1^b}}}{2I_{yy}}$$

Table 3.1: Longitudinal State Space Model Coefficients

3.2 PID Controllers

Proportional-Integral-Derivative (PID) control is a widely used feedback control technique that originates from classical control theory. Feedback control is a method of monitoring and correcting errors between desired and measured signals. Figure 3.2 contains a block diagram of the basic logic flow.

In Figure 3.2, there are four distinct signals: reference r, error e, control input u, and measured y. This project aims to control the angle of attack α such that there is a known time-sequence α_r used as the reference signal. Depending on controller attributes, the actual angle of attack may deviate noticeably from that which is desired - this is the measured signal. The difference between the desired and actual angles of attack make up the error e. The controller then takes in error e to determine the proper control input u necessary to correct the deviation. This is thrown into the plant which computes the state associated with the next time step (assuming a discretized system) which contains the measured angle of attack. The process is repeated for the entire time horizon.

The controller can be designed in a number of ways, even outside the realm of PID. Within, some systems only require P, PI, PD, etc. depending on the system attributes. For this project however, PID is necessary to handle the multitude of non-linearities such that short- and long-term behaviors are all addressed.

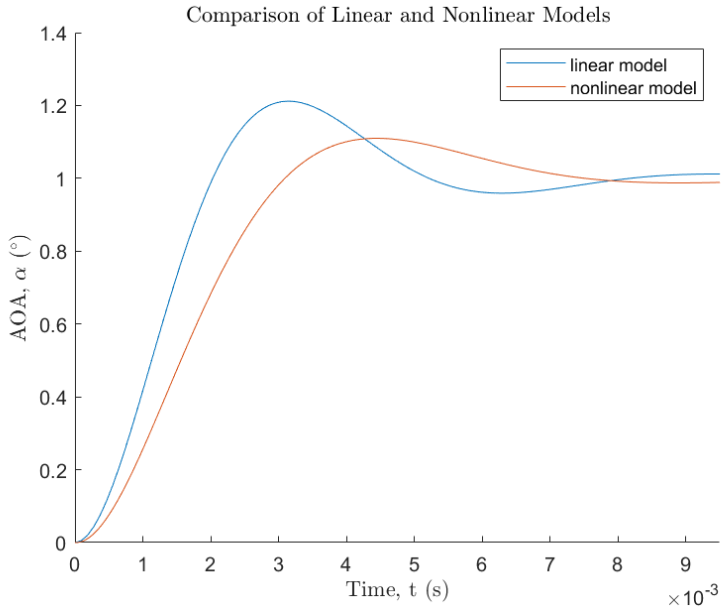

Figure 3.1: Simulation comparing the linear and nonlinear dynamics given the same set of control gains

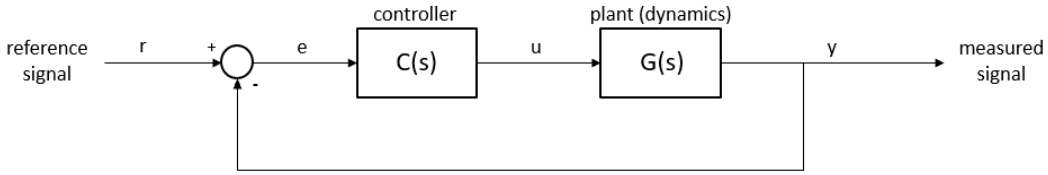

Figure 3.2: Block diagram of a typical feedback controller where signal e is the error and u is the control input

The block diagram in Figure 3.3 shows the control logic for processing the error signal in a PID controller. As the name suggests, there are three distinct paths: proportional, integral, and derivative, with equally suggestive purposes.

The first path takes the error and simply multiplies it by some gain, K_p. This is the first 'line of defense' in correcting any deviation between the desired and actual angles of attack. If this is non-zero, the controller will demand some control input that proportionally counter-attacks the deviation.

The integral path first integrates over the error signal for all time up until present before multiplying by some gain K_i. Counter to intuition, this term has strong long-term effects which ensure a steady-state at or near the desired angle of attack. By integrating over the entire preceding time horizon, if a deviation persists, this integral term grows stronger with time.

The third path takes the derivative of the error before multiplying by some gain K_d. This gives the controller some sense of short-term foresight by gauging how fast the error is moving away from or toward 0. If it is moving really quickly toward 0, this

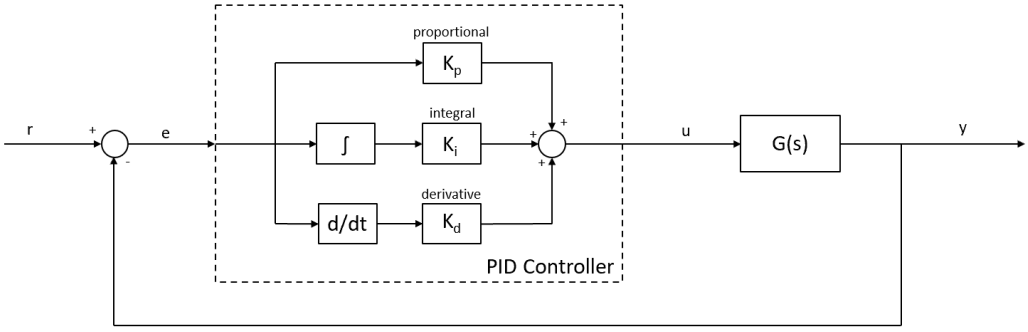

Figure 3.3: Block diagram of a PID-controlled feedback loop

term will slow the rate to minimize overshoot - essentially acting as a damper. The issues with the proportional gain is even if this rate is really high, K_p will continue to increase the rate. The derivative term compensates for this.

These paths are then summed to reveal one control input u. In the time domain, this signal will act as Equation 3.3.

$$u(t) = K_p e(t) + K_i \int_0^\tau e(\tau)d\tau + K_d \frac{de(t)}{dt} \tag{3.3}$$

In the frequency domain, the controller $C(s)$ is constructed in Equation 3.4.

$$C(s) = K_p + \frac{K_i}{s} + K_d s \tag{3.4}$$

The result is a harmony of gains acting as checks and balances of one another based on the error properties at any given time. There are many ways to determine what each should be including root-locus and empirical tuning. In this project, the MATLAB Simulink PID tuning tool is used a first guess on the linear system. Then they are fine-tuned empirically against the nonlinear model.

3.3 Gain-Scheduled PID Control

3.3.1 Gain Scheduling

A common technique used in high-speed aerial vehicles like missiles and rockets is gain-scheduled PID control. Such systems experience a wide variety of speeds and angles of attack such that non-adaptive controllers become ineffective. A gain-scheduled controller relies on sensor or feedback data to inform the tuning of the PID coefficients to maintain the stability and efficiency of the vehicle.

To visualize the importance of gain-scheduling, consider the simulations below in Figure 3.4. A PID controller was tuned to a step response for a projectile travelling at Mach 30 with an altitude of 0km (sea level). The corresponding gains were $K_p = 0.2$,

$K_i = 8$, and $K_d = 0.2$. This controller was applied to the projectile with the intended conditions (left) and when it is at an altitude of 20km (right).

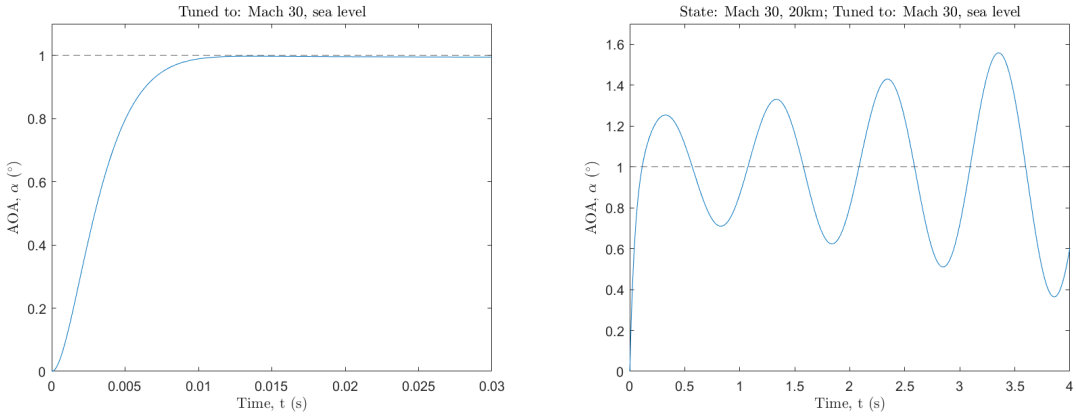

Figure 3.4: Left: step response of projectile held at Mach 30, sea level with a properly tuned controller; Right: step response of projectile held at Mach 30, 20km altitude with the same controller tuned to sea level

Starting with the properly tuned configuration, there is no overshoot in the specified time horizon and the 2% settling time is within 0.01 seconds. However, when applied to the configuration at an altitude of 20km, the system clearly diverges and has a much slower response time. This is not the desired behavior and is far from sufficient due to instability.

To understand the origins of this instability, the poles are observed using the linear model. In Table 3.2, Configuration 1 corresponds to the well tuned system while Configuration 2 is the undesired system. The poles are listed.

Configuration 1	Configuration 2
$-498.4 \pm 513.7i$	$-961.5 + 0i$
$-0.4836 \pm 6.323i$	$-38.35 + 0i$
	$0.02232 \pm 6.335i$

Table 3.2: Poles for the properly-tuned system (Configuration 1) and poles for the undesired system (Configuration 2), per the experiments in Figure 3.4

The poles in Configuration 2 confirm the instability observed in the step response with a pole in the right hand plane (RHP). In order for a system to be stable, all poles must be in the left hand plane (LHP) such that all real parts are negative.

It turns out that increasing the derivative gain for Configuration 2 will pull the unstable poles back across the imaginary axis to regain stability. If the gains are modified to $K_p = 0.2$, $K_i = 8$, and $K_d = 1.2$, then the response in Figure 3.5 results. This modification produces a stable response with very small over shoot and similar settling time to Configuration 1 - a desired behavior.

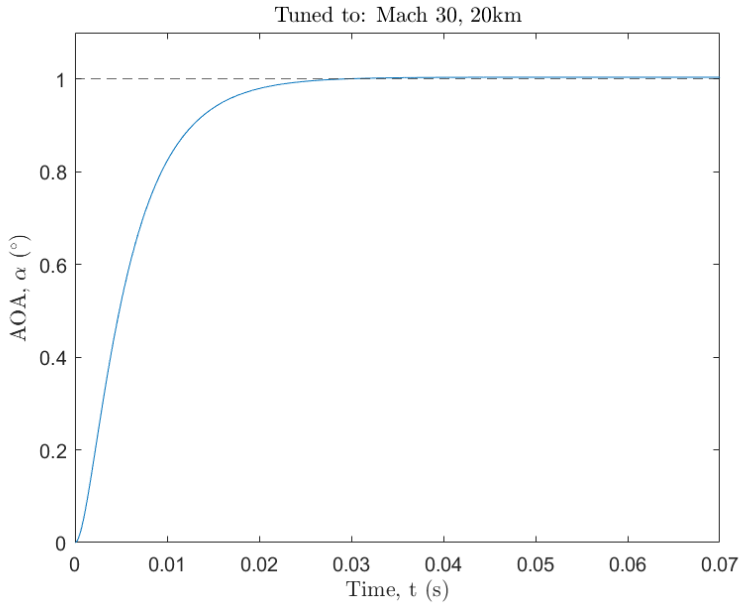

Figure 3.5: Step response for projectile and Mach 30, 20km altitude with PID gains $K_p = 0.2$, $K_i = 8$, and $K_d = 1.2$

It is clear that gain-scheduling can be a powerful tool when handling non-linearities. In aerospace, it is most typical to schedule based on Mach number and angle of attack. For systems that span a large range of altitudes, like an ascent vehicle, altitude can also be used.

This project uses Mach number and altitude to schedule gains via a look-up table. Mach number is incremented by 5 and altitude is incremented by 5km. Results are presented once stability criteria have been established.

3.3.2 Stability Criteria

Basic stability criteria are imposed to ensure consistency, efficiency, and robustness of the closed loop system. These come in two forms: time and frequency domain requirements. The latter is confirmed through observation of the linear model behaviors.

Below is a list of the requirements for each element of the gain-scheduled look-up table under the given set of conditions:

1. All closed-loop poles are in the LHP.
2. Percent overshoot is less than or equal to 2%.
3. Phase margin is greater than or equal to 60°.
4. Settling time is within 0.02 seconds.

The first is basic and necessary for achieving a stable system while criteria 3 defines specifically how stable and robust it must be. Criteria 2 and 4 define time domain behaviors which proved to perfectly harmonize the PID gains through empirical tuning. Each index of the look-up table achieves all four criterion.

Under these conditions, a set of gains was obtained for Mach values from 15 to 30 at intervals of 5, and altitudes from sea level to 50km at intervals of 5km. The proportional and integral gains experience minimal change such that the derivative term is primarily responsible for maintaining the desired behavior. Figure 3.6 graphically shows how K_d changes with the gain-scheduling variables.

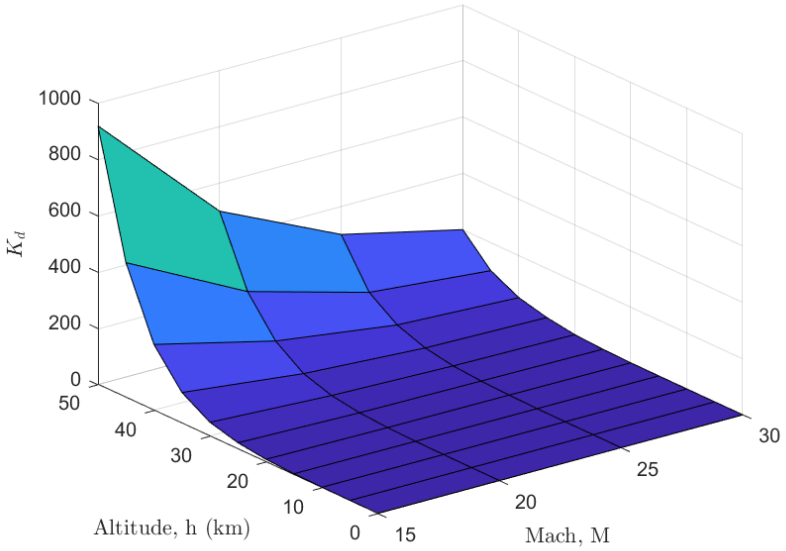

Figure 3.6: Gain-scheduled derivative gain values for specified look-up table set

For a given Mach value, K_d appears to increase exponentially with altitude. For higher Mach values, this exponential rise becomes less severe. The magnitude in which this gain increases can give rise to some issues at higher altitudes. Its' prevalence in the PID controller has the potential to overpower other terms that account for other important response behaviors. This phenomenon will be discussed further after implementation.

Chapter 4

Simulation

The simulation tool used in this study was MATLAB Simulink with initiation scripts written in MATLAB. This chapter explains the basic setup of the sim and how the logic flow mocks the ascent vehicle system. Up until this point, many topics have been introduced but it can be difficult to see how each piece fits with the next and why they are all important. The simulator is based on a previous project [3] and adapted to capture the dynamics and actuation of this particular setup.

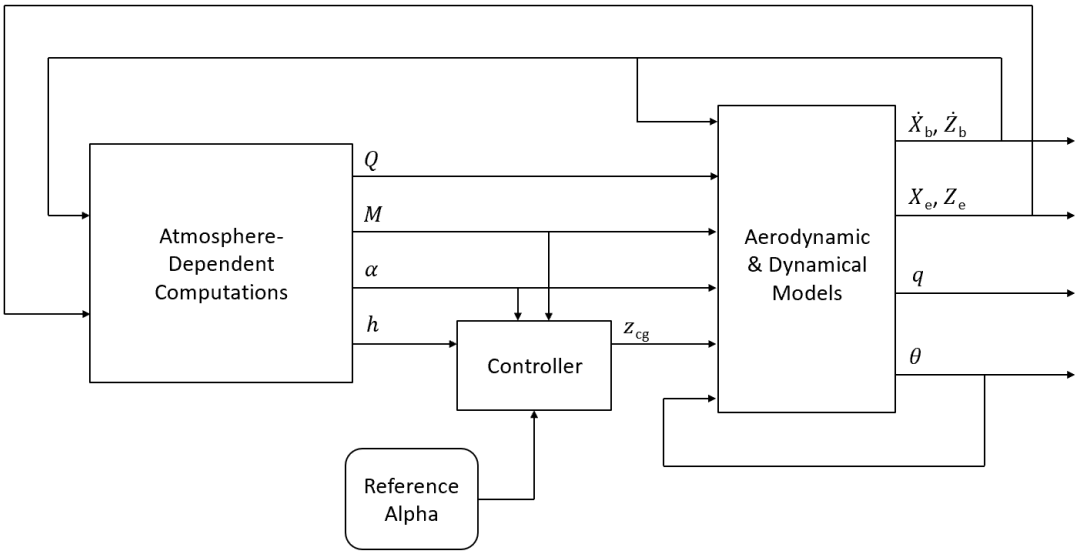

Figure 4.1: Highest level block diagram of ascent vehicle simulation

Figure 4.1 shows a block diagram describing the first and highest level of the simulation, capturing the complete feedback loop. There is only one input: 'Reference Alpha' which is the desired angle of attack sequence that the controller should track. The outputs include the body frame velocities $\dot{X}_b$ and $\dot{Z}_b$, the ECI frame position X_e and Z_e, the pitch rate q, and the attitude θ.

There are three primary components (blocks) which are in charge of processing their respective signals: Atmosphere-Dependent Computations, Controller, and Aero-

dynamic & Dynamical Models. Each will be discussed thoroughly in the following sections and draw from the setup previously presented.

4.1 Atmosphere-Dependent Computations

The first block, 'Atmosphere-Dependent Computations', uses the ISA model to compute applicable variables. This ensures that altitude is taken into account at each time step - this is necessary for a system spanning a large range of altitudes.

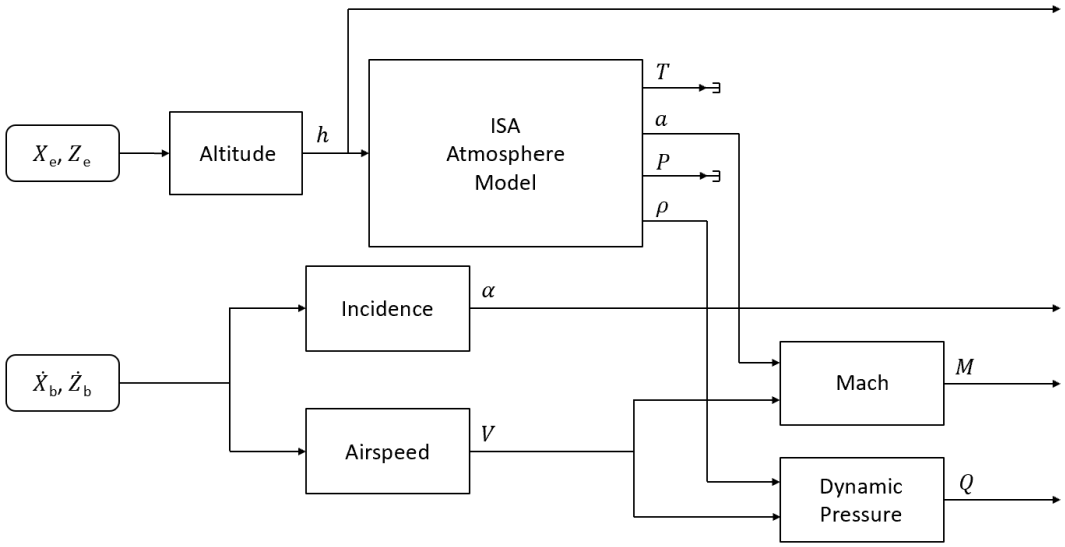

Figure 4.2: Simulation block diagram for variables depending on altitude

The inputs include the ECI frame position as well as the body frame velocities. The position is used to compute altitude by finding the resultant vector magnitude and subtracting the radius of the Earth (again, this assumes a perfectly circular Earth). This altitude, h is processed in the built-in MATLAB Simulink ISA Atmosphere Model block which yields temperature, T, speed of sound a, pressure P, and density ρ. The velocities are used to find the net airspeed V and angle of attack α. The aforementioned variables are used to compute Mach number and dynamic pressure as depicted in Figure 4.2. The resulting outputs are altitude, angle of attack, Mach number, and dynamic pressure.

4.2 Controller

The controller block (Figure 4.3) is responsible for computing a control demand that is appropriate for the given state relative to the reference signal. Similar to the feedback loop depicted in Figure 3.2, an error signal is computed by finding the difference

between the reference and measured angles of attack. This signal is processed in the PID controller, itself.

The Mach number and altitude serve as the determining parameters for the controller gains K_p, K_i, and K_d. These are indexed in the gain-scheduled look-up table as defined in Section 3. This process uses linear interpolation, and any extrapolation draws the closest data point. In the simulations discussed later, extrapolation is only used at high altitudes where moving mass control becomes ineffective.

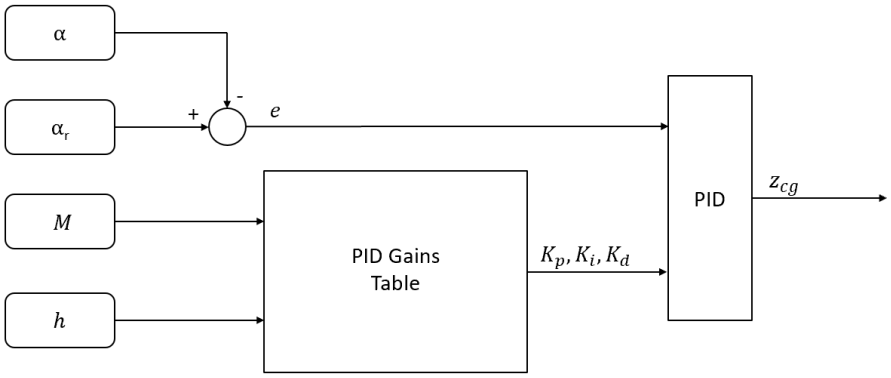

Figure 4.3: Simulation block diagram for controller compuations

4.3 Aerodynamic & Dynamical Models

Lastly, the aerodynamics and nonlinear dynamics update the feedback loop with the next state. The purpose of this block (Figure 4.4) is to take all the known data and fully understand the forces on the projectile such that the future may be predicted.

Knowing that the gravitational force vector must be pointed toward the center of the Earth, the ECI position of the projectile is used to determine the gravitational forces in this reference frame. This vector is broken up into its X and Z components as to be used later.

The Mach number and angle of attack are used to determine the aerodynamic coefficients via the look-up table compiled in Chapter 2 - this utilizes the same interpolation and extrapolation techniques as the controller look-up table. Assuming a constant reference area, the dynamic pressure is used to compute the aerodynamic forces acting on the projectile. These body frame forces are used to determine the moment about the center of gravity as a function of the axial distance between center of pressure and gravity, and control demand (normal position of the center of gravity).

Before throwing these forces into the nonlinear dynamics, they must be transformed to the ECI frame. While the moment stays the same, the axial and normal forces are converted to F_x^e and F_z^e via a direction cosine matrix (DCM) which takes in the attitude θ to complete the necessary rotation. To get the net ECI frame forces, these are summed with the respective gravitational forces such that the next state is

computed with the nonlinear dynamics. The outputs to this block are attitude, pitch rate q, ECI frame position, and body frame velocities.

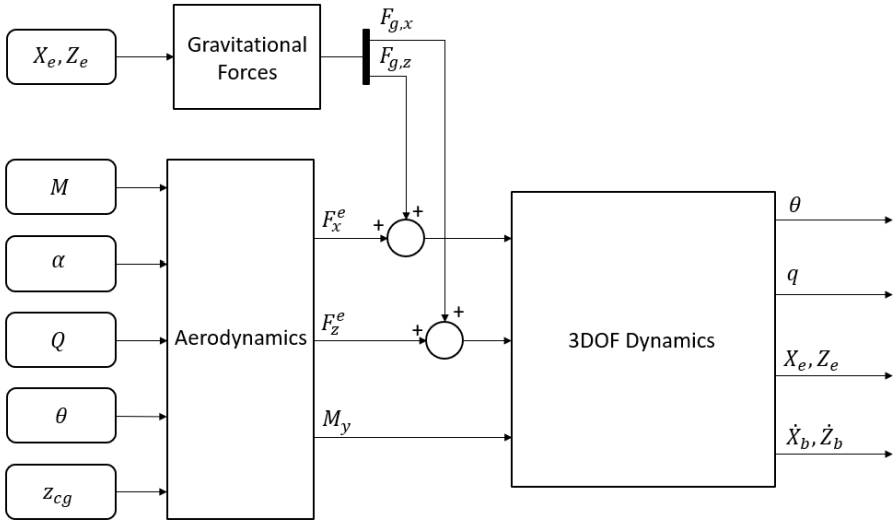

Figure 4.4: Simulation block diagram implementing aerodynamics and nonlinear dynamics.

4.4 Assumptions

A number of assumptions have been made in the making of this simulator and it is important to understand each before it is used for analysis. Below is a compiled list of all assumptions and simplifications used in this paper and incorporated in this simulator.

- The dynamics are 2-dimensional with 3 degrees of freedom (3DOF). While lateral dynamics will become important in projectile development, only the longitudinal are considered. This is sufficient for this thesis as ascent is the primary topic of discussion.

- The geometry of the projectile is simplified to a wedge. When this system is fully developed, the projectile will likely look nothing like a wedge and take on wave-rider properties with a cylindrical payload bay. This simplification allowed for easy computation of aerodynamic properties.

- The moment of inertia stays constant. In reality, the moment of inertia will change with the position of the moving mass. This change is considered negligible. Simulations will reveal that the moving mass only needs to occupy approximately one-fiftieth of the projectile mass, depending on its fixed axial position.

- The center of pressure remains fixed. In theory, the position of the center of pressure is undefined when the angle of attack is zero. This position also changes with angle of attack. Knowing that the projectile will span a small range of angles of attack, this assumption is made.
- The moving mass occupies the same axial position as the center of gravity. This simplification eliminates the need to model torques about the center of gravity due to the motion of the moving mass.
- The bandwidth of the actuator hardware is sufficient to complete all control demands. With a more thoroughly designed moving mass mechanism, limits can be incorporated into the simulator to reflect the actual hardware limitations. In the meantime, generous saturation and rate limits are implemented.

Chapter 5

Results

This chapter seeks to bring meaning to the work that has been presented thus far. The simulator, as described in Chapter 4, is applied to two sample trajectories which adhere to a set of fixed criteria. Important considerations are thoroughly investigated in order to motivate the trajectory design and weigh the feasibility of both. Additional trajectory variants are proposed which exceed the criteria but may offer more realistic insights into achieving orbit.

5.1 Sample Trajectories

To initiate each simulation, the projectile attributes are established such as geometry and balance parameters. Figure 5.1 shows the dimensions of the wedge: it will have a chord of 1.7m, a width of 0.6m, and a semi-apex angle of 10° - this is the same angle as that used to tabulate the aerodynamic look-up table. The initial mass and moment of inertia are 3000 kg and 3000 kg·m^2, respectively.

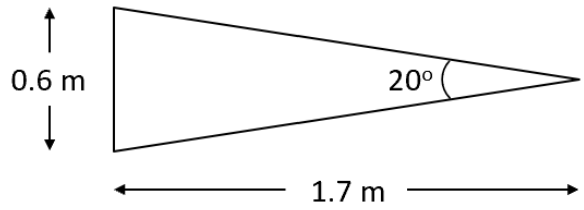

Figure 5.1: Simulation projectile dimensions

5.1.1 Design Criteria & Considerations

Before trajectory design can begin, design criteria must be established. Here, only initial and final conditions are considered. Under the specification of a linear impulse launcher, the following initial conditions apply:

1. Projectile starts at sea level ($h_0 = 0$).
2. Projectile starts with zero attitude and angle of attack ($\theta_0 = \alpha_0 = 0$).
3. Speed at launcher nozzle exit is Mach 30 ($M_0 = 30$).

In this study, only one final condition exists: projectile must be travelling at 7km/s or more when crossing the Karman line ($V_f \geq 7$km/s). While this is not necessarily a great metric for orbit feasibility, it serves as a control variable between trajectory types. Since moving mass control becomes ineffective at high altitudes and in space, other sources of actuation are necessary to enter orbit. This idea will be explored in the following sections.

With requirements established, there are a number of metrics that can motivate smart and realistic trajectory designs. Some of which are listed below.

- The atmosphere is relatively thick at altitudes under 20km. This has two implications: better maneuverability and more losses due to air friction in the lower atmosphere. When a moving mass is the only source of actuation, ambient pressure is critical for controllability; thus the control system will have more leverage where the pressure is higher. However, the longer the projectile stays in the lower atmosphere, the more kinetic energy it will lose to friction. This would require more momentum at launch to overcome.
- A maximum angle of attack should be established in consideration of heat shield stresses and overall stability. At higher angles of attack, the heat shield may experience more extreme stresses which expedite the ablation process. This will not only limit the life of the projectile but also produce stability concerns as the mass and geometry of the projectile rapidly change.
- As mentioned earlier, moving mass control cannot track in space due to the lack of atmosphere. To compensate, the projectile exit attitude should be minimized. This will reduce the amount of potential energy the projectile will need to store during launch and ascent. Although this metric is not included in the criteria for trajectory design, it should be a leading consideration to keep the system as simple as possible.

With all of this in mind, the following sections propose two sample trajectories which aim to minimize different parameters and tackle different issues.

5.1.2 Aggressive Approach

The first sample trajectory is considered aggressive and prioritizes reaching space as quickly as possible. An important feature of this approach is that the projectile will also get through the lower atmosphere in the quickest manner. Transferring this idea to an angle of attack reference signal, the projectile must pitch up quickly upon

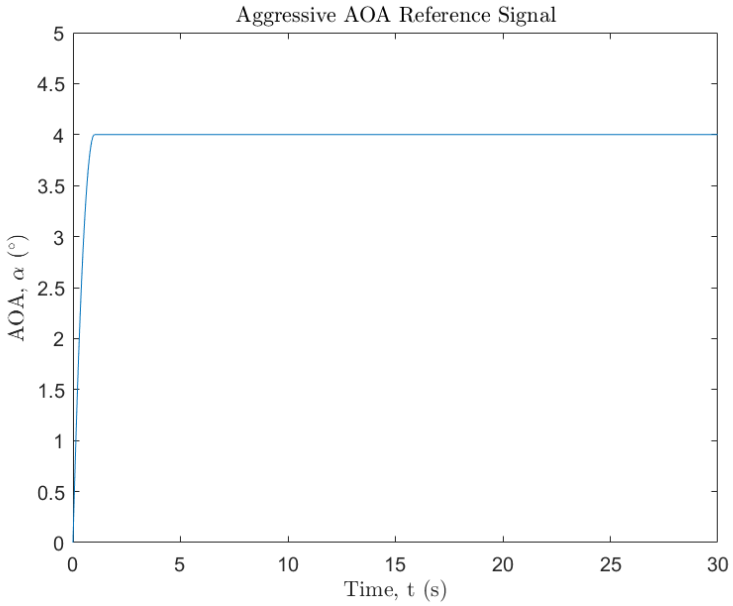

Figure 5.2: Reference angle of attack signal for aggressive trajectory

ejection and maintain the maximum angle of attack allowed; let this critical value be 4°.

The reference signal proposed in Figure 5.2 contains two components. The projectile is intended to take one second to reach the maximum allowable angle of attack. This gradual maneuver, compared to a true step response, will mitigate extreme accelerations of the moving mass. For the remainder of the trajectory until the projectile exceeds the Karman line, it will maintain this maximum value.

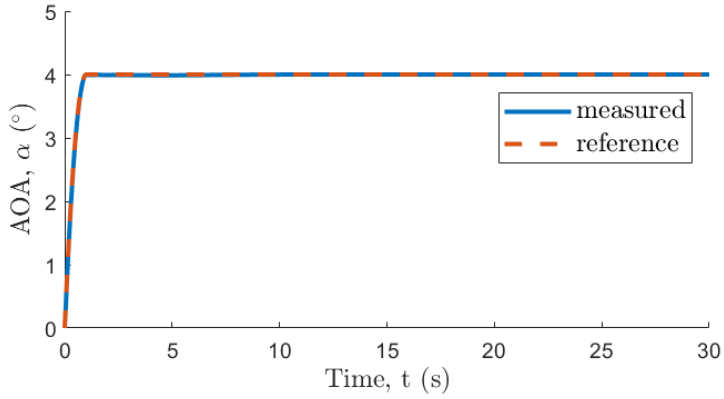

Figure 5.3: Aggressive approach simulation: comparison of measured and reference angle of attack

Figures 5.3 - 5.6 show the results associated with this trajectory. Starting with Figure 5.3, it is clear that the controller tracks the reference signal very well. Any deviation is hardly noticeable by eye.

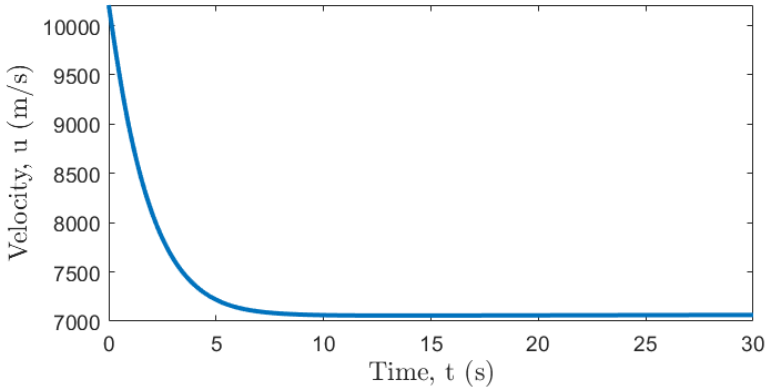

Figure 5.4: Aggressive approach simulation: axial velocity

Figure 5.4 proves that the final condition is met: the velocity at the Karman line (approximately 29 seconds) is greater than 7 km/s. Also important to note is how quickly the drop in velocity occurs - this essentially halts after 8 seconds. In the atmospheric model the pressure heavily drops off around 20 km. In this trajectory, the projectile crosses 20 km around 7 seconds (see Figure 5.5) which supports this previous observation.

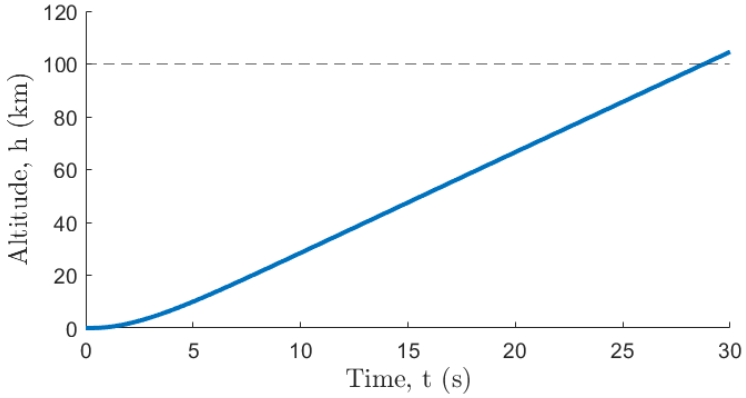

Figure 5.5: Aggressive approach simulation: altitude

Figure 5.6 shows the necessary control input in order to achieve the tracking in Figure 5.3. The implemented saturation limit is plus or minus 5 mm which is reached only at the beginning of the trajectory in the transition phase to $\alpha = 4°$. The change experienced in the remainder of the trajectory is due to the change in atmospheric conditions as the equilibrium state to maintain the angle of attack changes. Moreover, later in the trajectory, the derivative term in the PID controller becomes more prominent. This will become more apparent in the next ascent approach.

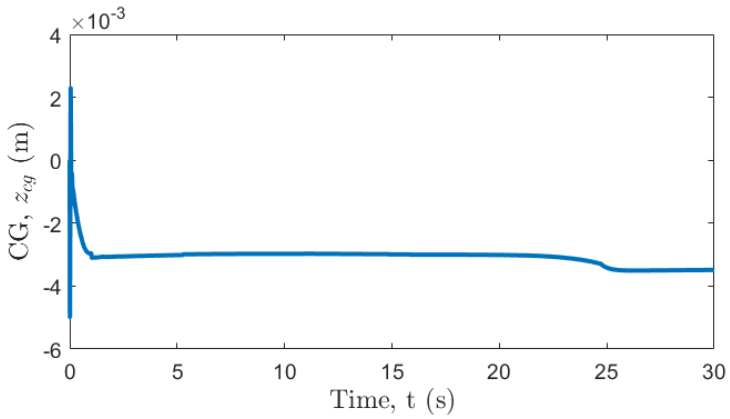

Figure 5.6: Aggressive approach simulation: center of gravity position

The primary issue with this trajectory is the incidence with the ground when the projectile crosses the Karman line; this angle is approximately 31°. As a result, the projectile will need to be capable of a rather large "delta-V" maneuver in order to enter LEO. Assuming that the reference signal is kept the same, a better metric for orbit feasibility may be setting a final condition such that the velocity normal to the altitude vector is greater than 7km/s. Let this velocity be defined by V_h for horizontal velocity.

Regardless of mass, if the projectile follows the same trajectory, it will lose the same amount of kinetic energy to air friction. So, if the momentum at ejection is increased, the projectile should maintain more speed through the atmosphere if it is more massive. A consequence of this is that the effect of the moving mass system will change slightly such that the projectile is more sluggish in its ascent, increasing ascent time and exposure to the atmosphere. Thus, the mass must be increased by nearly a factor of 2 to 5700kg in order to achieve the new final condition.

The results of this modification are shown in Figure 5.7. This solution shows that the projectile will take approximately 8 seconds longer to reach the Karman line but the control sequence remains relatively untouched. Despite the dramatic increase in mass, the controller performs very well in stabilization and tracking. However, there is some noticeable deviation between the reference and measured angles of attack once the max angle is reached. The gain-scheduled look-up table was tuned to the original configuration such that additional tuning is required to achieve the same level of performance with this new system.

This modified aggressive trajectory still poses issues: the vertical velocity (along the altitude vector) is substantial. A correction of almost 3km/s is required to enter a circular LEO. In comparison, the original trajectory would have required a correction of almost 4km/s.

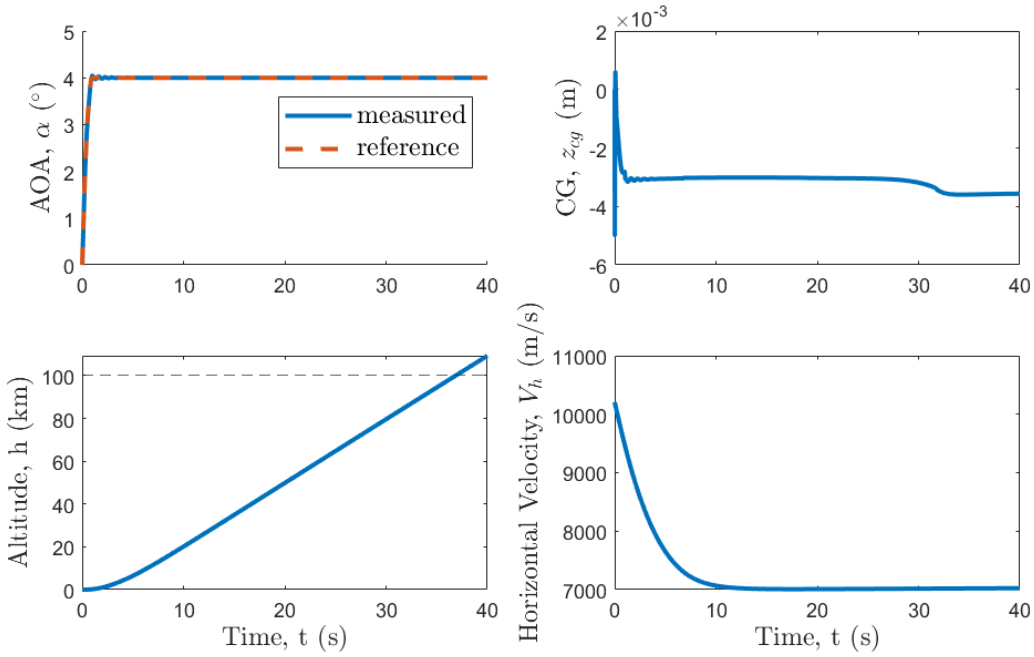

Figure 5.7: Modified aggressive trajectory simulation; top-left: measured and reference α, top-right: center of gravity position, bottom-left: altitude, bottom-right: horizontal velocity

5.1.3 Orbit-Conscious Approach

A smarter approach to reach orbit (not just space) would be to minimize projectile incidence as it crosses the Karman line. In this new design, the angle of attack is only maxed out for the first 5 seconds before switching to saturation in the negative direction. By making this switch at the 5 second mark, the projectile takes advantage of the ambient pressure below 20km before quickly exceeding the line to reduce friction losses. This reference signal is shown in Figure 5.8. Again, instead of using a step response between the two extremes, the control demand is reduced with a signal in the form of a quadratic.

Since the projectile is staying in Earth's atmosphere for a longer period of time due to the pitch down maneuver, it must be more massive to have the appropriate momentum capable of satisfying the final condition. The mass for this simulation (as well as moment of inertia) is increased to 4000kg.

Figures 5.9 - 5.12 summarize the results of this trajectory. Similar to the aggressive approach, the controller performs very well, closely tracking the reference signal. No deviation is visible to the eye in Figure 5.9.

Figure 5.10 shows that the final condition is met with margin. An interesting feature of this plot is the dip in velocity when the projectile switches to pitch down. This is to be expected as it spends more time under 20km. Figure 5.11 shows that the projectile crosses the 20km line around 8 seconds compared to the 7 seconds in the aggressive approach. The 1 second difference is enough to require the steep

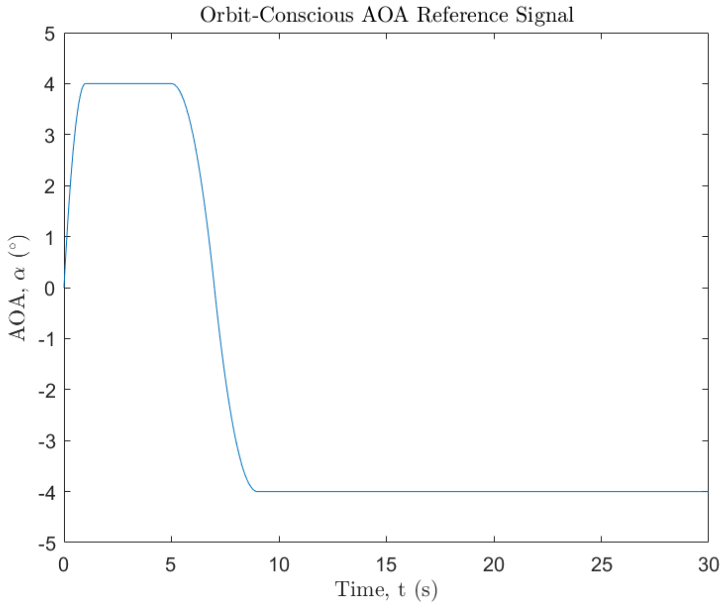

Figure 5.8: Reference angle of attack signal for orbit-conscious trajectory

momentum increase in this new approach. It also takes longer to cross the Karman line at approximately 36 seconds.

The control sequence required for this trajectory exhibits a number of interesting features. While it starts very similar to that in the aggressive approach, the 4 second switch between $4°$ and $-4°$ angle of attack causes some erratic motion. It is likely that the spikes are products of the balance between PID gains at high altitudes. The tuning process saw a dramatic increase in derivative gain with very little change in the proportional and integral gains. To put simply, these gains are meant to act as checks and balances of one another. When one overpowers the others, its flaws begin to show. In this case, the piece-wise nature of the reference signal 'confuses' the derivative controller as it attempts to predict the short-term behavior. Switching from a quadratic to a constant reference - despite having the same slope at this point - the derivative controller anticipates a desired increase in angle of attack and ends up undershooting. The controller then quickly compensates with a spike. To combat this, more stability criteria could be implemented such that the other gains experience more change with altitude.

As a quick sanity check, this plot also shows that the center of gravity position deviation from the chord of the projectile is the same in magnitude between the two extreme angle of attacks values. This is expected for a symmetric projectile such as a wedge.

To reduce the orbit correction needed to enter LEO, the same modification as in the aggressive approach is applied. In this case, the mass only needs to be increased to approximately 5700kg - the same as previously but with a much smaller percent increase. The implication here is that, to a certain point, the pitch down maneuver

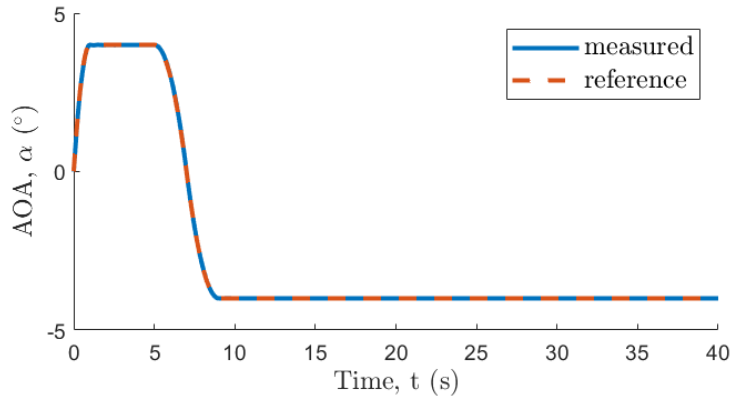

Figure 5.9: Orbit-conscious approach simulation: comparison of measured and reference angle of attack

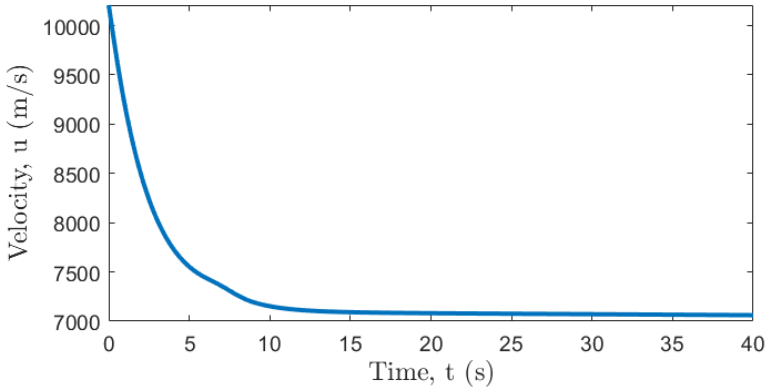

Figure 5.10: Orbit-conscious approach simulation: axial velocity

is just as effective in maintaining horizontal velocity as without. The pros and cons between the two approaches now heavily favor the orbit-conscious trajectory.

Figure 5.13 shows the simulation results for the modified orbit-conscious approach. There are some imperfections in the tracking response but less severe than in the previous case due to a smaller percent increase in mass. The ascent now takes about 45 seconds to reach the Karman line instead of 36 seconds but the horizontal velocity just narrowly missed the 7km/s mark.

The velocity correction that is required to enter orbit is about 2.3km/s compared to 3km/s for the unmodified trajectory. This results in a strong improvement from the aggressive case. However, this kind of correction is still sizeable and will require clever engineering solutions that minimize the complexity and need for propulsion systems. In this second sample trajectory, an example of a pitch down maneuver is provided to showcase the benefits. There are likely better trajectories which minimize mass and maximize horizontal velocity at the Karman line. One optimization technique in particular will be introduced in the next chapter.

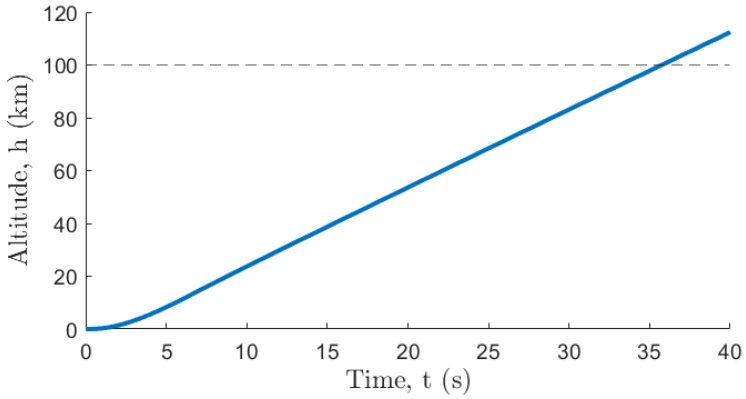

Figure 5.11: Orbit-conscious approach simulation: altitude

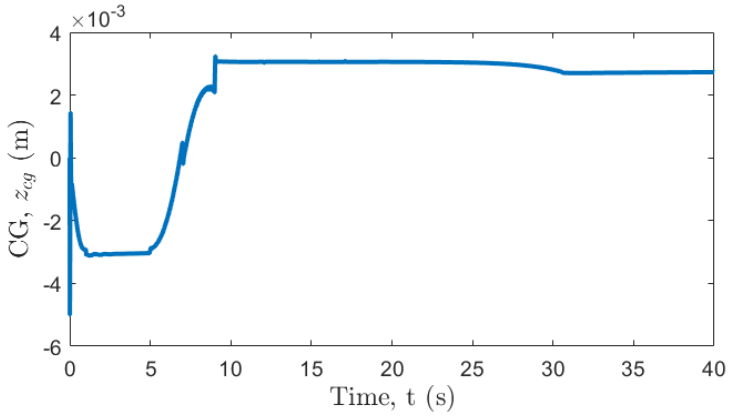

Figure 5.12: Orbit-conscious approach simulation: center of gravity position

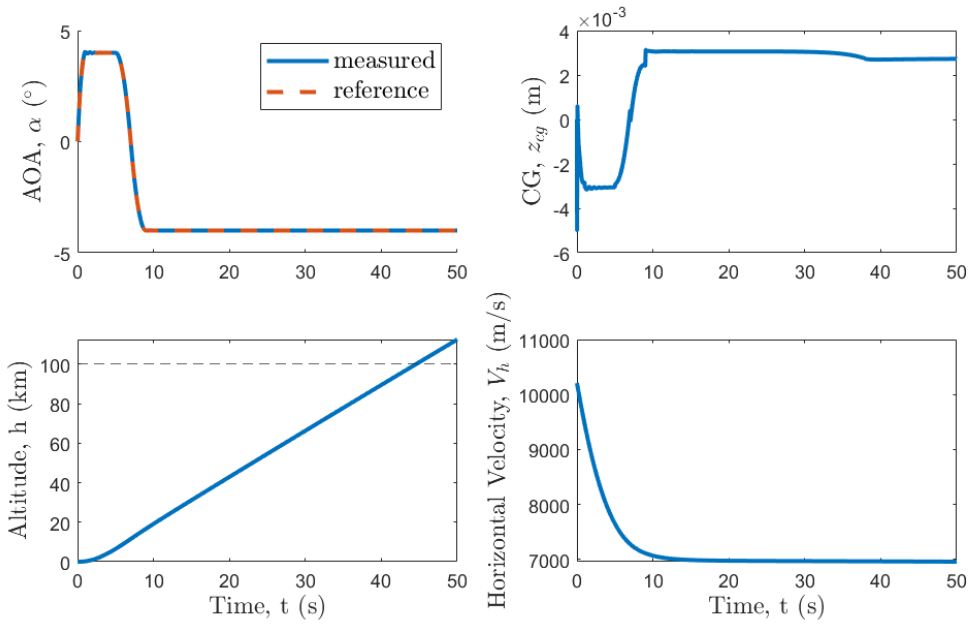

Figure 5.13: Modified orbit-conscious trajectory simulation; top-left: measured and reference α, top-right: center of gravity position, bottom-left: altitude, bottom-right: horizontal velocity

Chapter 6

Future work

This chapter describes the limitations and assumptions made in this thesis, and identifies directions that can be pursued in the short- and long-term to further complement its contributions. The work presented thus far is a narrow scope in a very large and complex problem that likely requires years, if not decades, to develop. The goal in the next few sections is to describe a basic road map about how to best tackle the rest of the problem.

6.1 Iterative Linear Quadratic Regulator

Chapter 5 revealed some room for improvement in trajectory design. An initial goal of this thesis was to understand the trajectory optimization process which could automatically compute desired trajectories. Investigation was conducted on iLQR (iterative Linear Quadratic Regulator) but was not successfully extended to this work as of this report.

The popular and well-studied optimization algorithm, LQR (Linear Quadratic Regulator), may be inadequate for these purposes. The issue is that it's best suited for linear systems and can falter with nonlinear systems, providing a sub-optimal solution. A variant of this algorithm is iLQR which was developed to understand non-linearities [15].

Assuming discretized dynamics, the cost function for this optimization problem is presented in Equation 6.1. Much of this setup mimics that of LQR with the exception of the terms δx_N and δu_k; this is where iteration becomes important. While LQR only conducts one backward and one forward pass of the solution, iLQR must conduct multiple until a threshold is reached. State improvement δx and input improvement δu are the differences between the previous and current iteration states and control sequence, respectively. Mathematically, that is $x^* = x + \delta x$ and $u^* = u + \delta u$.

$$J = \frac{1}{2}(x_N + \delta x_N - x^*)^T Q_f (x_N + \delta x_N - x^*) + \frac{1}{2}\sum_{k=0}^{N-1}(u_k + \delta u_k)^T R(u_k + \delta u_k) \quad (6.1)$$

The Hamiltonian shown in Equation 6.2 also exhibits iterative properties with matrices A and B changing with each step. These correspond to the linearized dynamics indexed by the current state, k; the dynamics are linearized at every time step.

$$H_k = \frac{1}{2}(u_k + \delta u_k)^T R(u_k + \delta u_k) + \delta\lambda_{k+1}^T(A_k\delta x_k + B_k\delta u_k) \tag{6.2}$$

The solution to this problem is more complicated than that in LQR. The input improvement is computed by solving the state and costate equations with the stationary condition. A thorough derivation is provided in [15]. The solution is provided in Equations 6.3-6.9.

$$\delta x_{k+1} = (I + B_k R^{-1} B_k^T S_{k+1})^{-1}(A_k\delta x_k - B_k R^{-1} B_k^T v_{k+1} - B_k u_k) \tag{6.3}$$
$$\delta u_k = -K\delta x_k - K_v v_{k+1} - K_u u_k \tag{6.4}$$
$$K = (B_k^T S_{k+1} B_k + R)^{-1} B_k^T S_{k+1} A_k \tag{6.5}$$
$$K_v = (B_k^T S_{k+1} B_k + R)^{-1} B_k^T \tag{6.6}$$
$$K_u = (B_k^T S_{k+1} B_k + R)^{-1} R \tag{6.7}$$
$$S_k = A_k^T S_{k+1}(A_k - B_k K) + Q \tag{6.8}$$
$$v_k = (A_k - B_k K)^T v_{k+1} - K^T R u_k + Q x_k \tag{6.9}$$

with boundary conditions

$$S_N = Q_f \qquad v_N = Q_f(x_N - x^*) \qquad dx_1 = 0$$

This system of equations must be solved in a specific order. First, the series S is computed by backwards recursion. K can then be computed at each step such that the series v is obtained by backwards recursion. The series dx can be solved forward. Everything is then known to get the series du. This process is repeated to refine the optimal control sequence.

Using this algorithm, it is possible that optimal ascent trajectories can be computed which prioritize the minimization of the projectile mass at ejection, and its incidence with the ground at the Karman line.

6.2 Proposed Road Map

6.2.1 Pressing Issues

Model Improvements

The main issues that can be tackled in the short-term are mostly eliminating the simplifying assumptions made for the simulation setup. These include:

- Recomputing the moment of inertia with the moving mass position.
- Accurately computing the center of pressure at every angle of attack.

- Accounting for the torque applied about the projectile center of gravity by the moving mass assuming there is some non-zero axial displacement.

These are relatively simple fixes that will add some complexities to the nonlinear and linear dynamics, alike. As such, they should be addressed first to prepare for larger issues down the road when more parameters are known.

With more comprehensive longitudinal dynamics defined, understanding the lateral dynamics and converting the current 3DOF model to 6DOF would be a natural next step. Depending on the geometry of the projectile, it may be necessary to develop more moving mass control schemes which travel along the other two axes (longitudinally and laterally).

Controller Improvements

There are two concerns regarding the current control system: the deviation between the linear and nonlinear models, and the effects of implementing a high derivative gain. The former is an integral part in the controller design process and is the main avenue in assessing performance. Understanding the exact sources of error and their level of influence is essential in verifying the nonlinear dynamics and the associated control design. This should be considered high priority when picking up this work.

Secondly, it is clear that the controller with respect to the nonlinear dynamics has flaws, especially at higher altitudes due to the magnitude of the derivative gain. It would be beneficial to explore alternative sets of stability criteria such that these behaviors are mitigated. This may entail loosening current requirements and incorporating entirely new ones.

Less pressing but still highly beneficial would be to develop a software which automatically tabulates the gain-scheduled look up table as a function of the system parameters and stability criteria. Empirical tuning can be a tedious process in projects of this nature and if multiple tables need to be constructed, automatic computation would drastically speed up the research process. This project would likely be contingent upon the accurate matching of the linear and nonlinear models.

Other

The implementation of iLQR in optimal ascent trajectory design would improve the assessment of projectile limitations as well as provide more insight into how best use Earth's atmosphere. The sample trajectories presented are very basic and serve as first guesses for the optimal trajectory. In fact, these could be used as the initial guess (iteration 0) of the iLQR computation process. Setting the weighting matrices Q and R to optimize different system attributes, local solutions can be computed.

Finally, the ability to track different variables like altitude will become a must. Since physical trajectory shapes were unknown in this work, tracking the angle of attack was the next best option. However, this is not the most practical approach in real flight because of the uncertainty in projectile final destination. Techniques

like successive loop closure as described in [7] can be used to track multiple variables using nested control feedback loops.

6.2.2 Long-Term Issues

These projects tend to be met with a lot of skepticism - and for good reason. There are several engineering challenges that have yet to be solved such that the most critical technology this system will rely on doesn't yet exist. However, this does not mean there is no feasible solution. Below is a brief list of challenges this project will inevitably face.

- The development of heat shield technology capable of withstanding the pressures and temperatures associated with Mach 30 flight at sea level. Due to the changing mass and geometry of the nose, the control system will require additional layers of complexity and robustness.
- The complete geometric design of the projectile. This will allow for the generation of an aerodynamic model based on experimental (preferred) or simulation data. This will likely be based on modern wave rider designs.
- Understanding the weight and balance of the projectile based on the geometry and layout. The moving mass system must remain unobstructed by all other payloads and instrumentation.
- The development of an actuation system other than moving mass which can lead the projectile to orbit. Some potential solutions include propulsion and spring loading of payloads.
- Designing the moving mass hardware setup. This will likely be some rail system which is actuated by a gear network. The saturation limits of this system will then need to be considered in the controller design.

Bibliography

[1] 3dof (body axes). https://www.mathworks.com/help/aeroblks/3dofbodyaxes.html. Accessed: 2024-04-14.

[2] atmosisa. https://www.mathworks.com/help/aerotbx/ug/atmosisa.html. Accessed = 2024-06-02.

[3] Design a guidance system in matlab and simulink. www.mathworks.com/help/stateflow/ug/designing-a-guidance-system-in-matlab-and-simulink.html. Accessed: 2024-06-02.

[4] Tonopah to be home to experimental hypersonic testing facility. https://pvtimes.com/tonopah/tonopah-to-be-home-to-experimental-hypersonic-testing-facility-130376/. Accessed: 2024-06-02.

[5] V-3 cannon. https://en.wikipedia.org/wiki/V-3_cannon. Accessed: 2024-06-02.

[6] John Anderson. *Fundamentals of Aerodynamics*. McGraw-Hill Education, 2017.

[7] Randal Beard and Timothy McLain. *Small Unmanned Aircraft*. Princeton University Press, 2012.

[8] Yu Gu, Guoxin Zhang, Ying Bi, Wenyue Mang, Xiaoping Ma, and Wenjun Ni. Pitch mathematical modeling and dynamic analysis of a hale uav with moving mass control technology. *Aerospace*, 2023.

[9] Tomislav Haus, Nikola Prkut, Katarina Borovina, Bruno Marić, Matko Orsag, and Stjepan Bogdan. A novel concept of attitude control for large multirotor-uavs based on moving mass control. *2016 24th Mediterranean Conference on Control and Automation (MED)*, 2016.

[10] Liang He, Tao Sheng, Krishna Dev Kumar, Yong Zhao, Dechao Ran, and Xiaoqian Chen. Attitude maneuver of a satellite using movable masses. *Acta Astronautica*, 2020.

[11] H. Husin, R.M. Mokhtar, A.A.A. Wahab, and N.Q.M Adnan. Achieving pitch control of fixed-wing aircraft through moving-mass control system. *Control, Instrumentation and Mechatronics: Theory and Practice*, 2022.

[12] Carl Knowlen and Adam Bruckner. Direct space launch using ram accelerator technology. *AIP Publishing*, 2001.

[13] D. J. Leith and W. E. Leithead. Survey of gain-scheduling analysis and design. *International Journal of Control*, 2000.

[14] Jianqing Li, Changsheng Gao, Chaoyong Li, and Wuxing Jing. A survey on moving mass control technology. *Aerospace Science and Technology*, 2018.

[15] Weiwei Li and Emanual Todorov. Iterative linear quadratic regulator design for nonlinear biological movement systems. *Pro- ceedings of the First International Conference on Informatics in Control, Automation and Robotics*, 2004.

[16] P. K. Menon, G. D. Sweriduk, E. J. Ohlmeyer, and D. S. Malyevac. Integrated guidance and control of moving-massactuated kinetic warheads. *Journal of Guidance, Control, and Dynamics*, 2004.

[17] Hanspeter Schaub and John Junkins. *Analytical Mechanics of Space Systems, Fourth Edition*. AIAA American Institute of Aeronautics Ast., 2018.

[18] Lee R. Scherer. Aerodynamic characteristics of a wedge and cone at hypersonic mach numbers, 1950.